




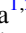






Long Live the Disk: Lifetimes of Protoplanetary Disks in Hierarchical Triple-star Systems and a Possible Explanation for HD 98800 B

María Paula Ronco^{1,2} , Octavio M. Guilera^{1,2,3} , Jorge Cuadra^{2,4} , Marcelo M. Miller Bertolami^{3,5} , Nicolás Cuello⁶ , Camilo Fontecilla^{1,2} , Pedro Poblete⁷ , and Amelia Bayo^{2,8} 

¹ Instituto de Astrofísica - Pontificia Universidad Católica de Chile, Av. Vicuña Mackenna 4860, Macul - Santiago, 8970117, Chile; mronco@astro.puc.cl

² Núcleo Milenio de Formación Planetaria (NPF), Chile

³ Instituto de Astrofísica de La Plata, CCT La Plata-CONICET-UNLP, Paseo del Bosque S/N (1900), La Plata, Argentina

⁴ Departamento de Ciencias, Facultad de Artes Liberales, Universidad Adolfo Ibáñez, Avenida Padre Hurtado 750, Viña del Mar, Chile

⁵ Facultad de Ciencias Astronómicas y Geofísicas, Universidad Nacional de La Plata, Paseo del Bosque S/N (1900), La Plata, Argentina

⁶ Univ. Grenoble Alpes, CNRS, IPAG (UMR 5274), F-38000 Grenoble, France

⁷ Astrophysikalisches Institut, Friedrich-Schiller-Universität Jena, Schillergäßchen 23, D-07745 Jena, Germany

⁸ Instituto de Física y Astronomía, Facultad de Ciencias, Universidad de Valparaíso, Chile

Received 2021 April 21; revised 2021 May 19; accepted 2021 May 20; published 2021 August 4

Abstract

The gas dissipation from a protoplanetary disk is one of the key processes affecting planet formation, and it is widely accepted that it happens on timescales of a few million years for disks around single stars. In recent years, several protoplanetary disks have been discovered in multiple-star systems, and despite the complex environment in which they find themselves, some of them seem to be quite old, a situation that may favor planet formation. A clear example of this is the disk around HD 98800 B, a binary in a hierarchical quadruple stellar system, which at an ~ 10 Myr age seems to still be holding significant amounts of gas. Here we present a 1D+1D model to compute the vertical structure and gas evolution of circumbinary disks in hierarchical triple-star systems considering different stellar and disk parameters. We show that tidal torques due to the inner binary, together with the truncation of the disk due to the external companion, strongly reduce the viscous accretion and expansion of the disk. Even allowing viscous accretion by tidal streams, disks in these kind of environments can survive for more than 10 Myr, depending on their properties, with photoevaporation being the main gas dissipation mechanism. We particularly apply our model to the circumbinary disk around HD 98800 B and confirm that its longevity, along with the current nonexistence of a disk around the companion binary HD 98800 A, can be explained with our model and by this mechanism.

Unified Astronomy Thesaurus concepts: [Protoplanetary disks \(1300\)](#)

1. Introduction

Stellar multiplicity is the most common outcome of star formation (Duchêne & Kraus 2013; Bate 2018), and it has been shown that the younger a stellar object is, the greater the probability that it is part of a multiple stellar system (Reipurth et al. 2014; Tobin et al. 2016).

As a by-product of their formation, young stellar objects are surrounded by disks of gas and dust called protoplanetary disks, where planet formation begins. Since the spectacular image of HL Tau (ALMA Partnership et al. 2015) more than 5 yr ago, the number of resolved disks around stellar objects of different kinds and ages has grown significantly. But protoplanetary disks have not only been found around single stars. Several surveys discovered many of them in binaries and even in higher-multiplicity star systems (Correia et al. 2006; Cox et al. 2017; Cieza et al. 2019; Manara et al. 2019; Akeson et al. 2019; Zurlo et al. 2020).

Some of the most recent and spectacular examples are the “cosmic pretzel” disk around the young [BHB2007] 11 binary system (Alves et al. 2019), the old polar circumbinary disk in the hierarchical quadruple-star system HD 98800 (Kennedy et al. 2019), and the spectacular disks imaged in the triple-star system GW Orionis (Kraus et al. 2020).

The evolution and lifetimes of disks in binary- or multiple-star systems are quite different from those of a protoplanetary disk around a single star. Circumbinary disks in close-in binaries are especially affected in the inner regions, which are

cleared out as a competition between the torques exerted by the inner binary that push the disk farther out and the viscous evolution trying to close this cavity (Artymowicz & Lubow 1994, 1996; del Valle & Escala 2012). The size of the cavity is estimated to be between two and five times the inner binary separation, increasing with the binary eccentricity (Artymowicz & Lubow 1994; Thun et al. 2017; Hirsh et al. 2020; Ragusa et al. 2020).

On the other hand, circumstellar disks orbiting only one of the stars in a binary system are truncated by the tidal effect produced by the outer star (Artymowicz & Lubow 1994). This truncation imposes a zero-flux edge condition at a distance from the central star estimated to be a function of the mass ratio and separation of the binary (Papaloizou & Pringle 1977; Pichardo et al. 2005).

For circumstellar disks, a mechanism that significantly contributes to a faster disk dispersal is photoevaporation. This phenomenon is produced by the central star (Alexander et al. 2006; Gorti et al. 2009) but also by possible external sources if the environment presents OB stars (Clarke 2007; Anderson et al. 2013; Winter et al. 2020) or the star suffers close encounters (Winter et al. 2018). The resulting circumstellar disk lifetimes are typically below 10 Myr (Fedele et al. 2010; Pfalzner et al. 2014). These effects also influence disk evolution in multiple stellar systems. In particular, circumbinary disks are expected to live longer than circumstellar disks (Alexander 2012), but truncated circumstellar disks in wide binaries could dissipate faster (Cieza et al. 2009; Kraus et al. 2012). In this context, two

questions are still under debate: (i) how does photoevaporation affect disk evolution in hierarchical triple stellar systems, and (ii) how do the abovementioned processes affect planet formation altogether?

Despite the complex dynamical environment where disks in binaries and triples form and evolve, planets can still form in them (Marzari & Thebault 2019). Indeed, more than 150 exoplanets have been discovered around binary-star systems and more than 30 in multiple-star systems of different kinds (Schwarz et al. 2016). Moreover, it has also been suggested that the frequency of planets in binary systems, particularly gas giants, can be as high as around single stars, except in the case of very close-in binaries (Martin 2018; Bonavita & Desidera 2020).

Hydrodynamical simulations play a key role in modeling with great detail the gas and dust evolution in protoplanetary disks. However, the high computational cost that these type of simulations require makes it not yet feasible to follow the whole disk evolution. For the moment, and despite their simplifications, 1D models close this gap, allowing us to study the evolution of protoplanetary disks until they completely dissipate.

In this work, we focus on describing the time evolution of protoplanetary disks in hierarchical triple-star systems with a new 1D+1D model that considers viscous accretion, irradiation, and X-ray photoevaporation from the inner binary. Our general aim is to compare their evolution with their circumbinary counterparts and determine their global characteristics and dissipation timescales for different stellar parameters.

A specific goal of this work is to understand the longevity of disks in hierarchical stellar systems. We then apply our model to the particular case of the disk in the hierarchical quadruple-star system HD 98800, which constitutes the ideal astrophysical test bed to do it, as it is uncertain how a nearly 10 Myr old disk still has significant amounts of gas (Ribas et al. 2018).

This paper is organized as follows. In Section 2, we describe our model for the evolution of disks in triple-star systems. We then define our general setup of initial conditions in Section 3. We describe our general results in Section 4, including a comparison between triple-star and binary-star disk evolution in Section 4.1 and a description of the stellar parameter dependency in Section 4.2. In Section 5, we describe the particular case of the system HD 98800 and apply our model to the disk around HD 98800 B. We present a discussion in Section 6 and conclude with some key aspects of our findings in Section 7.

2. Model for the Gas Disk Evolution in a Hierarchical Triple-star System

Here we present PLANETALP-B, a 1D+1D code that computes the time evolution of a gaseous disk in a hierarchical triple-star system. PLANETALP-B is an extension of our code PLANETALP (Ronco et al. 2017; Guilera et al. 2017, 2019, 2020; Venturini et al. 2020a, 2020b), a global model of disk evolution and planet formation that computes the growth of planets immersed in a circumstellar protoplanetary disk that evolves in time. This first version of PLANETALP-B, which can also be applied for the study of circumbinary disks and circumstellar disks around one of the stars in a wide binary-star system, only focuses on their gaseous component evolution.

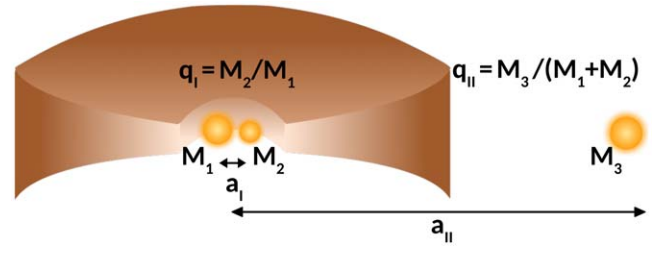


Figure 1. Schematic view of the configuration of our scenario of study: an axisymmetric circumbinary disk in a circular and coplanar hierarchical triple-star system.

2.1. The Vertical Disk Structure

Our subject of study is a disk in a hierarchical triple-star system, that is, a circumbinary disk affected by an external stellar companion. Figure 1 shows a schematic view of this configuration that, due to the axisymmetrical nature of our model, will always consider circular and coplanar orbits for the inner binary, the circumbinary disk, and the outer stellar companion. Moreover, despite the disk being subject to a time-dependent gravitational potential due to the stellar orbital motions, we consider the disk to be rotating in a gravitational potential given by the total mass of the inner binary system and neglecting the gravitational perturbations of the external companion. We will discuss the limitations of these considerations in Section 6.

To compute the vertical structure of a disk in this environment, we assume an axisymmetric, irradiated disk in hydrostatic equilibrium. We follow Guilera et al. (2017, 2019, 2020), who used the same methodology described in Alibert et al. (2005) and Migaszewski (2015) for a circumstellar case, but considering extra tidal heating terms in the energy equation due to the effects of the inner binary and the external companion (Lodato et al. 2009; Fontecilla et al. 2019). The complete set of equations is given by

$$\frac{\partial P}{\partial z} = -\rho\Omega^2 z, \quad (1)$$

$$\frac{\partial F}{\partial z} = \frac{9}{4}\rho\nu\Omega^2 + D_{\Lambda_I} + D_{\Lambda_{II}}, \quad (2)$$

$$\frac{\partial T}{\partial z} = \nabla \frac{T}{P} \frac{\partial P}{\partial z}, \quad (3)$$

where P , ρ , F , T , and z represent the pressure, density, radiative heat flux, temperature and vertical coordinate of the disk, respectively. Here $\nu = \alpha c_s^2 / \Omega$ is the viscosity (Shakura & Sunyaev 1973), where α is a dimensionless parameter, $c_s^2 = P/\rho$ is the square of the locally isothermal sound speed, $\Omega = \sqrt{GM_I/R^3}$ is the Keplerian frequency at a given radial distance R from the central binary, and $M_I = M_1 + M_2$ is its mass. We consider that the heat in the circumbinary disk is vertically transported by radiation or convection following the standard Schwarzschild criterion, as described in Guilera et al. (2019).

The terms $D_{\Lambda_I} = (\Omega_I - \Omega)\Lambda_I\rho$ and $D_{\Lambda_{II}} = (\Omega_{II} - \Omega)\Lambda_{II}\rho$ in Equation (2) represent the tidal heating dissipated in the form of radiation due to the inner binary and the outer stellar companion, respectively. Here Ω_I is the Keplerian frequency at the inner binary separation, a_I , given by $\Omega_I = \sqrt{G(M_I)/a_I^3}$, and Ω_{II} is the Keplerian frequency at the separation between the

inner binary system and the external companion star, a_{II} , computed as $\Omega_{\text{II}} = \sqrt{G(M_{\text{II}})/a_{\text{II}}^3}$, where $M_{\text{II}} = (M_1 + M_2) + M_3$, the total mass of the stellar system.

The quantities Λ_{I} and Λ_{II} represent the torques due to the inner binary and outer stellar companion, respectively. The classical expression for Λ proposed by Armitage & Natarajan (2002)⁹ for $q \ll 1$ could be overestimating the tidal torque contribution on the disks outside the Lindblad resonances, which may modify the surface density profiles (Tazzari & Lodato 2015). Thus, following Tazzari & Lodato (2015) and Fontecilla et al. (2019), we consider an exponential cutoff for the tidal torques outside this region, computed as

$$\Lambda_{\text{I}}(R) = \frac{f}{2} q_{\text{I}}^2 \Omega^2 R^2 \left(\frac{a_{\text{I}}}{\Delta_{\text{I}}} \right)^4 e^{-\left(\frac{R-R_{\text{OM}}}{W_{\text{OM}}} \right)^2}, \quad (4)$$

$$\Lambda_{\text{II}}(R) = -\frac{f}{2} q_{\text{II}}^2 \Omega^2 R^2 \left(\frac{R}{\Delta_{\text{II}}} \right)^4 e^{-\left(\frac{R-R_{\text{IM}}}{W_{\text{IM}}} \right)^2}, \quad (5)$$

where f is a dimensionless normalization parameter that can adopt different values between 0.001 and 1 (Armitage & Natarajan 2002; Alexander 2012; Vartanyan et al. 2016; Shadmehri et al. 2018). The variable q_{I} represents the mass ratio between M_2 and M_1 , and q_{II} is the mass ratio between M_3 and $(M_1 + M_2)$. Finally, $\Delta_{\text{I}} = \max(R_{\text{Hill}}^{\text{I}}, H_{\text{g}}, |R - a_{\text{I}}|)$ and $\Delta_{\text{II}} = \max(R_{\text{Hill}}^{\text{II}}, H_{\text{g}}, |R - a_{\text{II}}|)$, where $R_{\text{Hill}}^{\text{I}} = a_{\text{I}}(q_{\text{I}}/3)^{1/3}$ is the Hill radius of the secondary star in the binary system, $R_{\text{Hill}}^{\text{II}} = a_{\text{II}}(q_{\text{II}}/3)^{1/3}$ is the Hill radius of the third star, and H_{g} is the height scale of the disk. As in Fontecilla et al. (2019), we consider $R_{\text{OM}} = 1.59a_{\text{I}}$ and $R_{\text{IM}} = 0.63a_{\text{II}}$ to be the radii of the outermost and innermost Lindblad resonances and $W_{\text{OM}} = 75H_{\text{g}}$ and $W_{\text{IM}} = 370H_{\text{g}}$ to be the widths of the Gaussian smoothing.

Note that, if the case under study is that of a circumstellar disk, $\Lambda_{\text{I}} = \Lambda_{\text{II}} = 0$, while if it is a circumbinary disk, only $\Lambda_{\text{II}} = 0$, and if it is a circumstellar disk affected by an external star companion, only $\Lambda_{\text{I}} = 0$.

The boundary conditions at the surface of the disk H , $P_s = P(z=H)$, $F_s = F(z=H)$, and $T_s = T(z=H)$, considering the effects of the inner binary and outer star, are given by

$$P_s = \frac{\Omega^2 H \tau_{\text{ab}}}{\kappa_s}, \quad (6)$$

$$F_s = \frac{3\dot{M}_{\text{st}}\Omega^2}{8\pi} + \frac{((\Omega_{\text{I}} - \Omega)\Lambda_{\text{I}} + (\Omega_{\text{II}} - \Omega)\Lambda_{\text{II}})\dot{M}_{\text{st}}\Omega\mu m_{\text{H}}}{6\pi\alpha k_{\text{B}}(T_{\text{irr}}^4 + T_s^4)^{1/4}}, \quad (7)$$

$$0 = 2\sigma(T_s^4 + T_{\text{irr}}^4 - T_{\text{b}}^4) - \frac{9\alpha\Omega k(T_s^4 + T_{\text{irr}}^4)^{1/4}}{8\kappa_s\mu m_{\text{H}}} - F_s - (\Omega_{\text{I}} - \Omega)\frac{\Lambda_{\text{I}}}{2\kappa_s} - (\Omega_{\text{II}} - \Omega)\frac{\Lambda_{\text{II}}}{2\kappa_s}, \quad (8)$$

where $\tau_{\text{ab}} = 0.01$ is the optical depth, $T_{\text{b}} = 10$ K is the background temperature, and \dot{M}_{st} is the equilibrium accretion rate. In addition to the surface boundary conditions, due to

symmetry, we consider that the heat flux in the midplane of the disk should be $F(z=0) = F_0 = 0$.

Since we now have an inner binary system, the temperature associated with the stellar irradiation is considered as

$$T_{\text{irr}}^4 = T_{\text{irr1}}^4 + T_{\text{irr2}}^4; \quad (9)$$

i.e., we are adding up the fluxes due to each star, making the approximation that both are located at their center of mass, where

$$T_{\text{irr}_i} = T_i \left[\frac{2}{3\pi} \left(\frac{R_{*i}}{R} \right)^3 + \frac{1}{2} \left(\frac{R_{*i}}{R} \right)^2 \times \left(\frac{H}{R} \right) \left(\frac{d \log H}{d \log R} - 1 \right) \right]^{0.5}, \quad i = 1, 2, \quad (10)$$

and R_{*i} and T_i are the radius and effective temperature of the primary ($i=1$) and secondary ($i=2$) stars of the inner binary system, R is the radial coordinate, and $d \log H / d \log R = 9/7$. The individual stellar masses, with their corresponding stellar radii and temperatures, are obtained from Baraffe et al. (2015). Note here that our model does not consider the possible effect of self-shadowing if the disk becomes nonflared or the possible irradiation from the third star.

Equations (1)–(3) of the vertical structure are computed using a shooting method with a Runge–Kutta–Fehlberg integrator, while Equations (6)–(8) are solved by a multi-dimensional Newton–Raphson algorithm. Solving these equations allows us to obtain the mean viscosity $\bar{\nu}(\Sigma_{\text{g}}, R)$, where Σ_{g} is the gas surface density, required to solve the radial evolution of the disk.

It is worth noting that the detailed computation of the vertical structure and the thermodynamical quantities of circumbinary disks in hierarchical triple-star systems can be particularly useful for future transfer radiative calculations.

2.2. Time Evolution of the Radial Disk Structure

In order to compute the time evolution of the gas surface density, we solve the classical 1D diffusion equation (Pringle 1981), including the terms corresponding to the torques injected by the binaries, already described in the previous subsection,

$$\frac{\partial \Sigma_{\text{g}}}{\partial t} = \frac{3}{R} \frac{\partial}{\partial R} \left[R^{1/2} \frac{\partial}{\partial R} (\bar{\nu} \Sigma_{\text{g}} R^{1/2}) - \frac{2\Sigma_{\text{g}}(\Lambda_{\text{I}} + \Lambda_{\text{II}})}{3\Omega} \right] + \dot{\Sigma}_{\text{w}}(R), \quad (11)$$

where t is the temporal coordinate, $\bar{\nu}$ is the mean viscosity at the midplane of the disk, Σ_{g} is the gas surface density, and $\dot{\Sigma}_{\text{w}}(R)$ is the sink term due to the X-ray photoevaporation. The latter is computed following the analytical prescriptions derived by Owen et al. (2012) from radiation-hydrodynamic models (Owen et al. 2011, 2012). The total mass-loss rate depends on the X-ray luminosity of the central star, which in our case is actually a binary. Therefore, we use

$$L_{\text{X}} = L_{\text{X}}^1 + L_{\text{X}}^2, \quad (12)$$

where L_{X}^1 and L_{X}^2 are the X-ray luminosities of the stars of the inner binary system, which can be computed following

⁹ For a detailed discussion of this prescription, we refer the reader to Petrovich & Rafikov (2012), Rafikov & Petrovich (2012), and Rafikov (2016).

Preibisch et al. (2005),

$$\log(L_X^i [\text{erg s}^{-1}]) = 30.37 + 1.44 \log\left(\frac{M_i}{M_\odot}\right), \quad i = 1, 2, \quad (13)$$

who derived this correlation between X-ray luminosity and stellar mass for young ($5 < \log \tau [\text{yr}] < 9.5$) low-mass stars ($M_\star \leq 2 M_\odot$). Then, as described in Appendix B of Owen et al. (2012), for primordial disks (or disks without holes), the total mass-loss rate is given by

$$\dot{M}_w = 6.25 \times 10^{-9} \left(\frac{M_1}{1 M_\odot}\right)^{-0.068} \times \left(\frac{L_X}{10^{30} \text{erg s}^{-1}}\right)^{1.14} M_\odot \text{yr}^{-1}, \quad (14)$$

while for disks with holes or transition disks, it is given by

$$\dot{M}_w = 4.8 \times 10^{-9} \left(\frac{M_1}{1 M_\odot}\right)^{-0.148} \times \left(\frac{L_X}{10^{30} \text{erg s}^{-1}}\right)^{1.14} M_\odot \text{yr}^{-1}. \quad (15)$$

These approximations were derived for circumstellar disks that can present both kinds of morphologies at different epochs. However, circumbinary disks always present inner cavities; thus, we only compute the X-ray mass-loss rate following Equation (15).

From the normalized radial mass-loss profiles derived by Owen et al. (2012) and presented in their Appendix B, and by computing \dot{M}_w (from Equation (15) in our case), we can compute $\dot{\Sigma}_w(R)$ that verifies

$$\dot{M}_w = \int 2\pi r \dot{\Sigma}_w(R) dR. \quad (16)$$

As in Rosotti & Clarke (2018), we are not considering the possible contribution from the external companion to the photoevaporation rate of the circumbinary disk. The choice to only consider X-ray photoevaporation in our model is due to the fact that this type of irradiation has yielded much higher photoevaporation rates than the extreme-UV (EUV) rates (Ercolano & Owen 2010; Owen et al. 2011; Picogna et al. 2019). Moreover, Kunitomo et al. (2021) recently showed that this is the predominant disk dispersal mechanism for low-mass stars ($< 2.5 M_\odot$), compared to EUV and far-UV photoevaporation (see their Figure 11).

An important point to mention here is that, in the 1D approach, the form of Equations (4) and (5) completely prevents viscous gas accretion onto the stars. However, as shown by Artymowicz & Lubow (1996) and many others (e.g., Cuadra et al. 2009; Dunhill et al. 2015; Tang et al. 2017), accretion onto the stars still happens via tidal streams, a mechanism that can only be captured in 2D and 3D simulations. This mass-loss rate is not constant but modulated by the binary orbit. While MacFadyen & Milosavljević (2008) estimated that this accretion could be an average of $\sim 10\%$ of the one expected in the absence of the binary, D’Orazio et al. (2013) and Farris et al. (2014) suggested that it could reach up to 30%–60%. The results of Ragusa et al. (2016) are in

agreement with these previous works when the disk is thick. However, these authors found that it is possible to suppress all mass accretion if the disk becomes sufficiently thin. Due to the uncertainties on the amount of this mass loss, our model allows that a certain fraction ϵ of the expected accretion rate is accreted by the inner binary. In a similar way as Alexander (2012), we compute the accretion rate \dot{M}_B as $\dot{M}_B = 3\pi\nu\Sigma_g$ at every radial bin between R_c and $2R_c$ (where R_c is the radius of the inner cavity) and adopt the maximum value of \dot{M}_B in that region, considering it as an upper limit.

The disk radial structure is solved using an implicit Crank–Nicholson method from a_I to a_{II} using 2000 radial bins logarithmically equally spaced. We set boundary conditions of zero torque, which is equivalent to having zero density at the boundaries. We note here that the boundary conditions are applied to the radial bins corresponding to a_I and a_{II} . However, as we show in the next sections, the tidal torques included in the model naturally truncate the disk at different locations. A validation of our 1D+1D model for the case of circumbinary disks is presented in Appendix A, comparing our results to those of Vartanyan et al. (2016).

3. Initial Conditions and General Setup

The initial gas surface density profile for our protoplanetary disk is given by

$$\Sigma_g = \Sigma_g^0 \left(\frac{R}{R_0}\right)^{-\gamma} e^{-(R/R_0)^{2-\gamma}}, \quad (17)$$

where R_0 is the characteristic radius of the disk, γ is the gas surface density exponent, and Σ_g^0 is a normalization parameter that depends on the disk mass.

The inner and outer radii of our circumbinary disk are set initially equal to the star separations, a_I (inner binary) and a_{II} (outer binary). However, the inner and outer radii of the disk will naturally evolve (expand and contract, respectively) as a consequence of the tidal torques induced by the inner binary and external star (represented by the term that includes Λ_I and Λ_{II} in Equation (11)).

We define a general setup of initial conditions, in which we fix the protoplanetary disk parameters and only vary the stellar ones. As shown in Table 1, we perform simulations for a fixed disk of $M_d = 0.05 M_\odot$, with $R_0 = 39$ au, $\gamma = 1$,¹⁰ and $\alpha = 10^{-3}$. Our fiducial simulation (T1) considers $q_I = 1$ ($M_1 = M_2 = 0.5 M_\odot$), $a_I = 0.5$ au, $q_{II} = 1$ ($M_3 = 1 M_\odot$), and $a_{II} = 100$ au. We also perform simulations with different q_I (and thus different M_1 and M_2), q_{II} , a_I , and a_{II} in order to test the dependency of the results on these parameters. The total mass of the inner binary system is always set to $M_1 = 1 M_\odot$, so the disk dynamical time is the same for all models.

4. General Results

In this section, we first present the main differences between the disk evolution of our fiducial case in a triple-star system and the same disk in a binary-star system not affected by an external companion. We then describe the results and general characteristics of the simulations of Table 1, where we consider different stellar parameters for triple-star systems.

¹⁰ These are typical values obtained for circumstellar disks (Andrews et al. 2010).

Table 1

Stellar Parameters Considered for Our General Simulations of a Fixed Disk of $M_d = 0.05 M_\odot$, $R_c = 39$ au, $\gamma = 1$, and $\alpha = 10^{-3}$ and the Resulting Disk Properties, Such as the Dissipation Timescale τ , Cavity Size R_c , and Truncation Radius R_t for the Case that Considers Viscous Accretion by Tidal Streams with an Efficiency of 30%

Case	Simulation	Stellar Parameters							Simulation Results ($\epsilon = 30\%$)		
		$M_1 [M_\odot]$	$M_2 [M_\odot]$	q_I	a_I [au]	$M_3 [M_\odot]$	q_{II}	a_{II} [au]	τ [Myr]	R_c [au]	R_t [au]
Binary test case	B1	0.5	0.5	1	0.5	4.47	1.65	...
Fiducial case	T1	0.5	0.5	1	0.5	1	1	100	3.58	1.65	34.50
q_I dependency	T2	0.67	0.33	0.5	0.5	1	1	100	3.38	1.32	34.50
	T3	0.91	0.09	0.1	0.5	1	1	100	2.80	0.85	34.50
q_{II} dependency	T4	0.5	0.5	1	0.5	0.5	0.5	100	3.80	1.65	42.30
	T5	0.5	0.5	1	0.5	0.1	0.1	100	4.17	1.65	63.5
a_I dependency	T6	0.5	0.5	1	1.5	1	1	100	3.57	4.82	34.50
	T7	0.5	0.5	1	2.5	1	1	100	3.38	7.85	34.50
a_{II} dependency	T8	0.5	0.5	1	0.5	1	1	500	4.35	1.65	168
	T9	0.5	0.5	1	0.5	1	1	1000	4.36	1.65	300

4.1. Disk Evolution: Triple-star versus Close Binary-star Systems

It has been previously shown that circumbinary disks dissipate at a lower rate than circumstellar disks (Alexander 2012). However, what happens to disks in triple-star systems? To address this question, we performed two simulations: our fiducial case T1 (see Table 1), which represents a circumbinary disk in a triple hierarchical system, and B1, which is exactly the same but ignoring the external star, thus representing an isolated circumbinary disk. We recall that, in terms of our model, the latter is achieved by setting $\Lambda_{II} = 0$.

4.1.1. Without Accretion by Tidal Streams

In order to focus on how the disk density profile changes with time, we first do not allow any gas accretion via streams to occur in these simulations. Recall from the end of Section 2.2 that, in 1D models, the form of the torque given by Equation (4) prevents any mass loss by viscous accretion unless accretion by tidal streams is allowed. Thus, the disk only loses mass by photoevaporation. Since the mass-loss rate due to the X-ray photoevaporative winds only depends on the X-ray luminosity of the central object (see Equation (15)), and since T1 and B1 systems have the same disk mass and inner stellar pair, the dissipation timescale for both disks is exactly the same. However, the shapes of the density profiles are quite different. In terms of our model, a gas disk has completely dissipated when its mass in our simulations is lower than $1 \times 10^{-6} M_\odot$. If, as in this case, the disk mass only evolves due to X-ray photoevaporation, the dissipation timescale can be directly estimated without the need of performing simulations by computing L_X in Equation (12) and then \dot{M}_w in Equation (15). For both B1 and T1, $q_I = 1$ and $M_1 = M_2 = 0.5 M_\odot$; thus, we obtain $\dot{M}_w \approx 8.9 \times 10^{-9} M_\odot \text{ yr}^{-1}$, and both disks dissipate in $\tau \approx 5.6$ Myr.

Figure 2 shows the time evolution of the gas surface density (top), temperature (middle), and aspect ratio (bottom) profiles for the disk of our fiducial case (T1) in a hierarchical triple-star system (left column) compared to the same disk in a binary

system (B1; right column) and, for both cases, without any mass loss by viscous accretion.

The differences between the disk profiles in the triple and binary systems are remarkable. At early times (0.5 Myr of evolution; red lines) and due to the injection of angular momentum by the inner binary, the inner radius of the gas disk expands, creating an inner cavity of up to ~ 1.65 au ($\sim 3.30 a_I$, as is expected from previous studies; e.g., Artymowicz & Lubow 1994) for both cases, while the outer radius presents different values. In T1, the effect of the outer stellar companion located at 100 au prevents disk expansion beyond ~ 35 au, which represents $\sim 0.35 a_{II}$ and is in agreement with previous studies (Papaloizou & Pringle 1977; Pichardo et al. 2005). This situation is different for the circumbinary case, B1, where the disk can freely expand beyond ~ 100 au. As a natural consequence of this expansion, the maximum value reached by the gas surface density profile is lower than that for the one in the triple-star system by about a factor of ~ 0.5 , and this difference increases with time, although the mass for both cases evolves at the same rate (i.e., each comparable, same-color profile between T1 and B1 presents the same amount of mass).

While the gas density profiles in T1 evolve slowly in a confined region without significantly changing their shape, in B1, the gas disk is pushed further out, generating a growing cavity as a simultaneous consequence of photoevaporation and disk expansion due to angular momentum conservation (see Figure 3 for a comparison between the evolution of the inner cavity sizes). In addition, the gas surface density profiles in B1 decay faster than in T1, thus decreasing the local available mass of gas inside ~ 35 au. As an example, at 4 Myr, the gas surface density at 10 au is $\sim 10 \text{ g cm}^{-2}$ for B1, while it is $\sim 200 \text{ g cm}^{-2}$ for T1. This situation could favor gas-giant planet formation in triple-star systems, in which a protoplanet can spend more time embedded in the gas disk compared to a circumbinary disk. However, it is important to note that higher gas surface densities can also enhance inward migration of low- and intermediate-mass planets.

An interesting point here is that, as a consequence of the higher gas surface density profiles for T1, the midplane

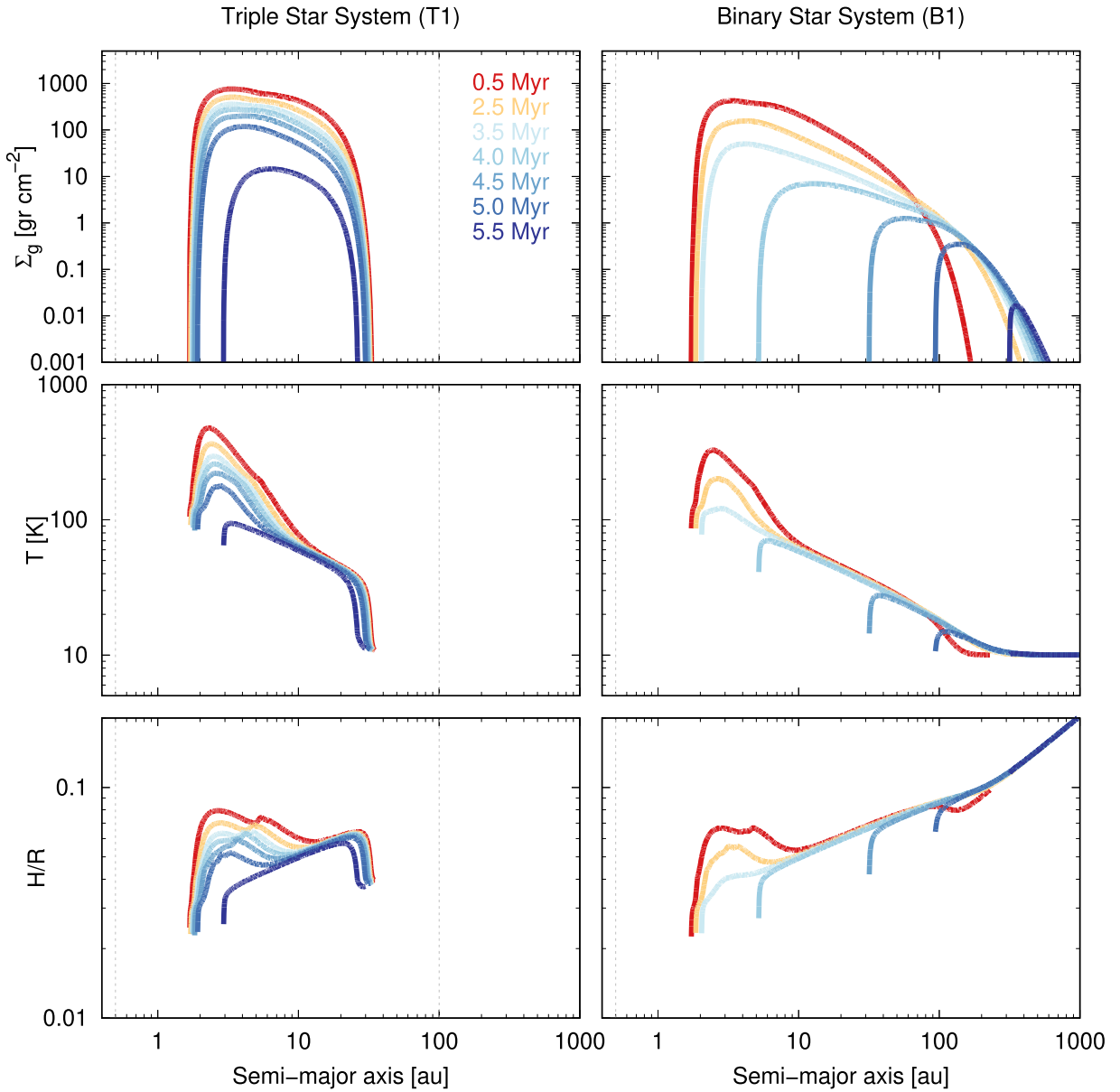


Figure 2. Time evolution for the gas surface density (top), temperature profiles (middle), and aspect ratio (bottom) of our fiducial disk (T1) in the hierarchical system (left) and for the same disk in the binary-star system (B1) not affected by an external companion. Different color profiles represent the gas disk at different ages. The inner gray vertical dashed lines represent the separation between both stars of the inner binary system, and the outer lines (only for T1) represent the separation between the inner binary and the external star.

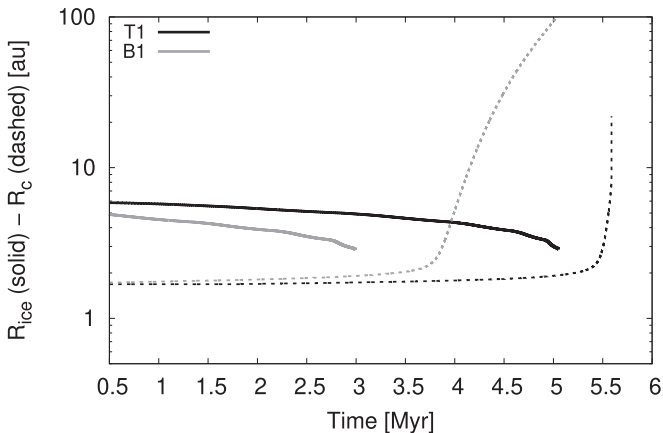


Figure 3. Time evolution of the location of the ice line (solid lines) and the inner radius or cavity size (dashed lines) for T1 and B1.

temperature and aspect ratio profiles of the same disk are higher than those of B1. These quantities could play an important role in the solid-component evolution of these protoplanetary disks and thus in the process of planet formation, since higher gas densities also imply higher dust densities. As an example, the location of the water-ice line (~ 170 K), beyond which an increment in the solid surface density is expected, is always further out in T1 compared to B1, and it also lasts longer, as can be seen in Figure 3. This situation may lead to the formation of ice cores in T1 for longer timescales and at larger distances than in B1. In addition, higher aspect ratios reduce the migration rate of low- and intermediate-mass planets (e.g., Paardekooper et al. 2011; Jiménez & Masset 2017) and increase the pebble isolation mass (e.g., Lambrechts et al. 2014). These two effects could help planet formation in hierarchical triple-star systems more than in binaries.

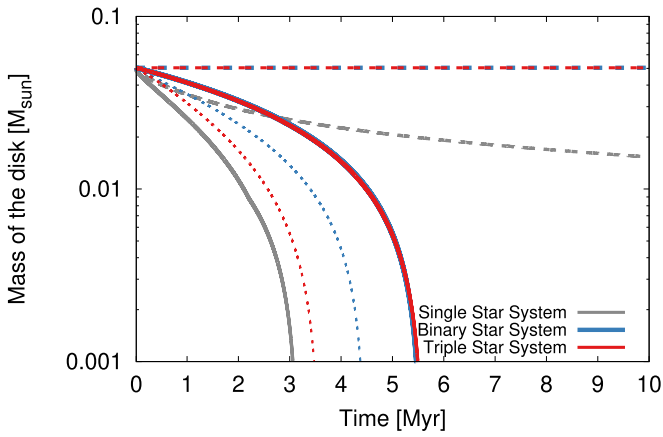


Figure 4. Time evolution of the mass of the disk of our fiducial case T1 in a hierarchical triple-star system (red curves) and in the circumbinary case B1 (blue curves). The mass evolution for the corresponding circumstellar disk case is represented in gray. The initial mass of the disk in this case is $M_d = 0.05 M_\odot$. The solid lines denote the cases in which the photoevaporation due to the inner binary is included, while the long-dashed lines represent the cases in which it is not. The short-dashed lines in red and blue represent the mass of the disks in the triple and binary systems, respectively, with photoevaporation and an accretion efficiency by streams of 30%.

On the other hand, we note that while the temperature radial profiles are similar in both cases, i.e., they decrease as we move away from the central binary, the aspect ratio profiles present more differences. This is particularly important for self-shadowing, although we reiterate here that this effect is not included in the disk thermodynamics of our model. In any case, self-shadowing would be stronger in the case of the triple than the circumbinary-star system. In the latter case, the decrease in the aspect ratio could generate an effect of self-shadowing until ~ 10 au, leading to a cooler disk between ~ 2 and ~ 10 au than previously computed. This effect would be negligible after 2.5 Myr. For the disk in the triple-star system, self-shadowing would affect it until ~ 20 au at early times and persist until ~ 4.5 Myr of the disk evolution.

4.1.2. With Accretion by Tidal Streams

In this section, and in order to understand how the differences between the T1 and B1 profiles affect the disk dissipation timescales, we now allow some mass loss due to viscous accretion via streams to occur. For this comparison, we adopt an efficiency of 30%, which is an intermediate value between those found by MacFadyen & Milosavljević (2008) and D’Orazio et al. (2013). The general shape and size of the gas, temperature, and aspect ratio profiles are very similar to the ones with no mass loss by viscous accretion presented in Figure 2. However, they no longer dissipate on the same timescale; the disk in B1 dissipates in 4.47 Myr, while the one in T1 dissipates in 3.58 Myr, $\sim 80\%$ of the circumbinary disk lifetime. The reason is quite simple and directly related to the behavior of the gas disk profiles. As described at the end of Section 2.2, the mass-loss rate due to the accretion by tidal streams is proportional to Σ_g inside $2R_c$, which is always greater in T1. Thus, the mass removal is higher for the disk in the triple-star system, though still slow enough to possibly allow planet formation.

Figure 4 shows the time evolution of the mass of the disk in the triple-star system T1 in red, the disk in the binary system B1 in blue, and, as a reference, the time evolution of the

corresponding circumstellar¹¹ disk in gray, which, for the purposes of our model, is computed with $\Lambda_I = \Lambda_{II} = 0$. Both the solid and long-dashed lines represent cases in which accretion via streams was not considered, and the short-dashed lines represent cases in which we consider an accretion efficiency of 30% by streams. In particular, the long-dashed lines represent cases in which photoevaporation is not included. In this figure, it can be clearly seen that, if photoevaporation is not included, the mass loss by viscous accretion is completely suppressed in B1 and T1; thus, the disks would remain intact forever. This is, as mentioned before, a consequence of the form of the torques for 1D models. Then, if we now consider photoevaporation, both the disks in B1 and T1 dissipate on the same timescale because they are only losing mass due to this mechanism. The dissipation timescale changes between B1 and T1, as previously described, when we also allow mass loss by viscous accretion by tidal streams with an efficiency of 30%. The disk mass evolution is, in this case, represented by the short-dashed lines. Although for the triple-star system, the dissipation timescale is shorter than for the binary case, it is still longer than for the corresponding circumstellar disk (solid gray line).

4.2. Stellar Parameter Dependency

We now describe the global results of the simulations of Table 1 for disks that evolve due to photoevaporation and viscous accretion by tidal streams with an efficiency of 30%.

4.2.1. Dependence on the Stellar Mass Ratios

In this section, we vary the masses of the stars but always keep the total mass of the inner stellar binary set to $M_I = 1 M_\odot$.

We first consider three different values for the mass ratio between components M_1 and M_2 . In models T1, T2, and T3, we set $q_I = 1, 0.5,$ and $0.1,$ respectively. The mass ratio q_I of the inner binary plays a key role in the models. On the one hand, q_I enters in Equation (4). Thus, the higher the mass ratio, the greater the torque imparted by the binary to the disk, and, consequently, the wider the inner cavity and the narrower the disk, since the external star always truncates the disk at ~ 30 au. The different cavity sizes of the disks can be appreciated in Table 1. On the other hand, different mass ratios imply different individual masses for the inner system, and, given the nonlinear relation of X-ray luminosity with mass, a different total L_X . Therefore, as q_I grows, L_X decreases, and, consequently, so does the mass-loss rate due to photoevaporation (see Equation (15)). Thus, the disk dissipates faster in systems with lower values of q_I . The differences, however, are not very significant and can be found in Table 1. The time evolution of the density profiles of T2 and T3 can be seen in the first column of Figure 5.

To analyze the dependence of the results on q_{II} , we performed two simulations, T4 and T5, with $q_{II} = 0.5$ and $0.1,$ respectively, in addition to our fiducial case T1 with $q_{II} = 1$. Different values of q_{II} do not play any role in the photoevaporation process, since the masses of the inner binary do not change in these simulations; thus, the size of the inner cavity remains the same as for T1. What does change in this

¹¹ The inner radius of the circumstellar disk is also defined at 0.5 au, as for the case of B1 and T1, in order to be consistent with the comparison. Moreover, to have exactly the same mass-loss rate due to the X-ray photoevaporation, the central star is assumed to have the same X-ray luminosity as the inner binary system of B1 and T1.

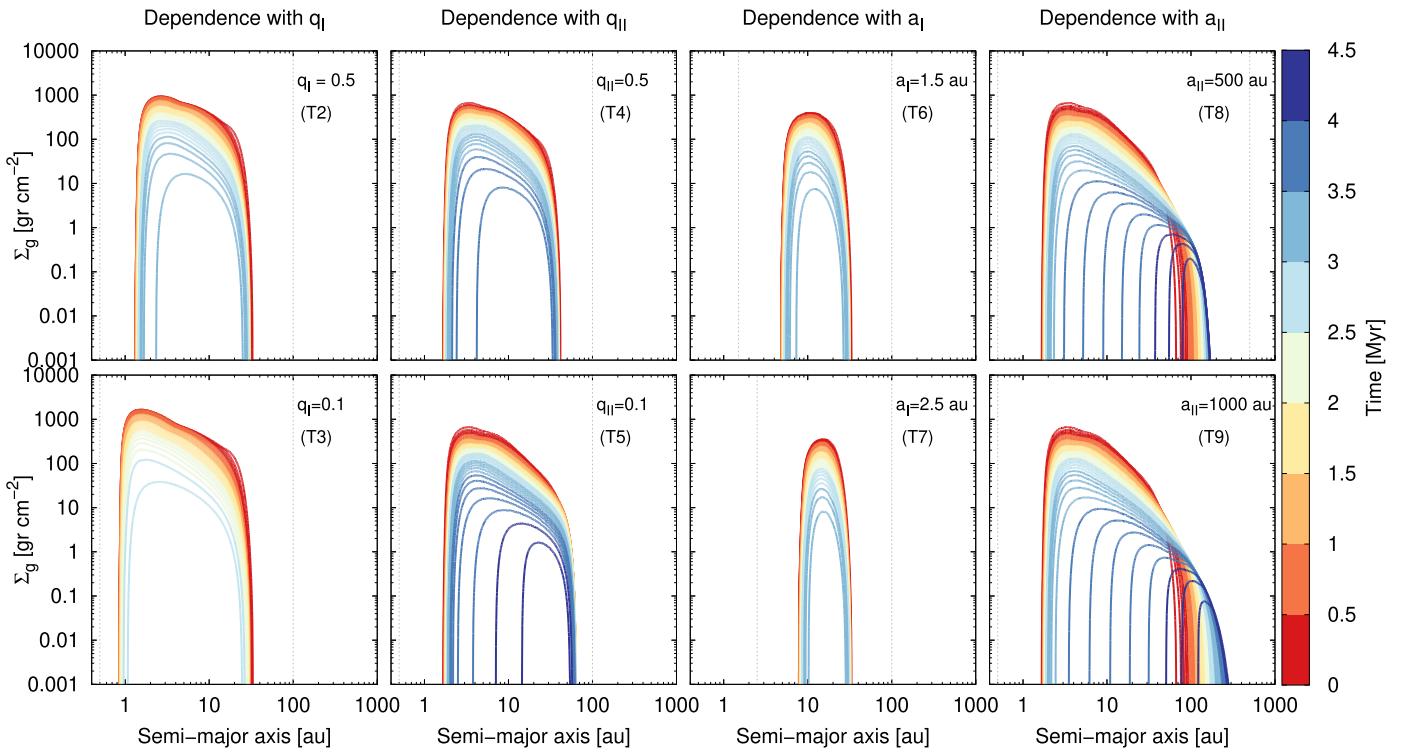


Figure 5. Time evolution, represented by the color scale, of the gas surface density profiles for simulations T2–T9 that present different values of q_I (first column), q_{II} (second column), a_I (third column), and a_{II} (fourth column). The inner gray vertical dashed lines represent the separation between both stars of the inner binary system, and the outer lines represent the separation between the inner binary and the external star.

case is the mass of the external companion. The main effect of q_{II} is that, as this parameter decreases, the torques exerted by the outer companion to the disk are weaker (see Equation (5)); thus, the gas disk is able to expand more (see Table 1). This expansion consequently causes the surface density profiles to decrease; therefore, there is less mass loss by viscous accretion by streams. The time evolution of the density profiles for these cases can be seen in the second column of Figure 5.

4.2.2. Dependence on the Semimajor Axes

We now test the dependency of the results on a_I and a_{II} , keeping all stellar masses fixed as in the fiducial case T1. We performed two simulations, T6 and T7, with $a_I = 1.5$ and 2.5 au, in addition to our fiducial case T1 with $a_I = 0.5$ au. The effect produced by the increase of the inner binary separation is to create a wider inner cavity due to a higher injection of angular momentum to the disk (see Equation (4)). Consequently, the disk is confined to evolve in an outer and narrower region, since the external stellar companion, located at 100 au, truncates the disk at ~ 35 au. Despite the widths of the three cases being different, the dissipation timescales are practically the same, as can be appreciated in Table 1. This happens because the larger the cavity, the smaller the gas surface density at the location where \dot{M}_B is computed but the higher the viscosity as it increases at greater distances from the central star. This increment in \mathcal{V} is a consequence of its proportional dependence on c_s and H_g . Therefore, $\dot{M}_B \propto \mathcal{V} \Sigma_g$ remains roughly constant, and the accretion rates are very similar for the three cases, while at the same time, photoevaporation affects the disk equally in the three cases.

Finally, we run two simulations with different values for a_{II} . Apart from T1 that has $a_{II} = 100$ au, T8 and T9 have $a_{II} = 500$

and 1000 au, respectively. In this case, the effect of increasing the separation between the inner binary and the outer stellar companion allows the disk to evolve in a more extended region. This expansion of the disk reduces the gas surface densities compared to T1, producing lower mass-loss rates due to viscous accretion by streams, which, as already mentioned, is proportional to Σ_g . Therefore, the dissipation timescales of these disks are longer than the one of T1 (~ 3.58 Myr). However, the differences between the dissipation timescales of T8 and T9 are insignificant (see Table 1). Recall from Section 4.1.2 that B1, which represents the circumbinary disk case, dissipates in ~ 4.47 Myr. Thus, disks in triple-star systems with sizes larger than ~ 500 au tend to evolve and dissipate in the same way and on similar timescales as the corresponding circumbinary case.

5. The Quadruple Hierarchical System HD 98800

The hierarchical quadruple stellar system HD 98800 is part of the TW Hya association (Soderblom et al. 1996; Torres et al. 2008; Ducourant et al. 2014). It is formed by two spectroscopic binaries, Aa–Ab (a single-line spectroscopic binary, or SB1) and Ba–Bb (a double-line spectroscopic binary, or SB2; Torres et al. 1995), and a narrow circumbinary disk that orbits the well-characterized system Ba–Bb. The system Ba–Bb is formed by two stars of ~ 0.6 and $\sim 0.7 M_\odot$ with a semimajor axis of about 0.5 au and a high eccentricity estimated to be ~ 0.78 (Boden et al. 2005). The orbit of the system Aa–Ab is instead more uncertain, although it could have a total mass similar to that of Ba–Bb, of $\sim 1.3 M_\odot$ (Tokovinin 1999), but probably with a lower mass ratio being an SB1 (Torres et al. 1995). The estimated separation between both binary systems is ~ 45 au, and their mutual orbit presents an eccentricity of

Table 2
Disk Parameters Considered for the Particular Case of HD 98800 B and the Corresponding Results for Setup 1 and Setup 2

Simulation	Disk Parameters		Setup 1				Setup 2							
			Efficiency				Efficiency							
	M_d [M_\odot]	α	R_c [$a_{\text{Ba-Bb}}$]	R_t [$a_{\text{A-B}}$]	τ [Myr]	τ [Myr]	τ [Myr]	τ [Myr]	R_c [$a_{\text{Ba-Bb}}$]	R_t [$a_{\text{A-B}}$]	τ [Myr]	τ [Myr]	τ [Myr]	τ [Myr]
Sim 1	0.01	10^{-2}	2.18	0.51	>10*	2.78	1.24	0.82	2.25	0.49	>10	1.75	0.77	0.51
Sim 2	0.01	10^{-3}	3.38	0.30	>10*	8.31	4.49	3.21	3.15	0.31	>10	4.46	2.17	1.50
Sim 3	0.01	10^{-4}	5.12	0.18	>10*	>10*	9.26	7.19	4.21	0.22	>10	8.15	4.41	3.18
Sim 4	0.05	10^{-2}	2.06	0.55	>10	3.59	1.51	0.97	2.01	0.56	>10	2.15	0.90	0.59
Sim 5	0.05	10^{-3}	2.96	0.32	>10	>10*	6.27	4.27	2.85	0.33	>10	6.22	2.77	1.86
Sim 6	0.05	10^{-4}	4.48	0.21	>10	>10	>10*	>10*	3.89	0.24	>10	>10	6.17	4.26
Sim 7	0.1	10^{-2}	2.02	0.57	>10	3.81	1.57	1.01	1.96	0.59	>10	2.55	0.94	0.61
Sim 8	0.1	10^{-3}	2.84	0.33	>10	>10*	6.81	4.58	2.72	0.35	>10	6.78	2.96	1.98
Sim 9	0.1	10^{-4}	4.23	0.21	>10	>10	>10*	>10*	3.77	0.25	>10	>10	6.77	4.62

Note. Both setups were computed using the estimated X-ray luminosity of the system by Kastner et al. (2004). For setup 1, we adopt $a_{\text{Ba-Bb}} = 0.5$ and $a_{\text{A-B}} = 45$ au, and for setup 2, we adopt $a_{\text{Ba-Bb}} = 0.9$ and $a_{\text{A-B}} = 27$ au. Here τ represents the dissipation timescale of the disk in megayears, and R_c is the radius of the inner cavity and R_t the outer truncation radius, both measured at $\Sigma_g = 10^{-3}$ g cm $^{-2}$ and 0.05 Myr of evolution and expressed in $a_{\text{Ba-Bb}}$ and $a_{\text{A-B}}$ units. The resulting timescales greater than 7 Myr are highlighted in bold, and simulations with asterisks are those that better fit the current mass and age of HD 98800 B.

about 0.4 (Tokovinin et al. 2014). Additionally, the inclination of the outer binary Aa–Ab with respect to the circumbinary disk was estimated to be $\approx 88^\circ$, and the circumbinary disk is in a polar configuration with respect to Ba–Bb (Kennedy et al. 2019).

The age of this quadruple system is estimated to be between 7 and 10 Myr (Kastner et al. 1997; Prato et al. 2001; Barrado Y Navascués 2006; Ducourant et al. 2014), which is quite old for a protoplanetary disk. Moreover, since there was no detected emission at near-IR wavelengths, the circumbinary disk in HD 98800 B was thought to be a debris disk for many years (Olofsson et al. 2012). Recently, Ribas et al. (2018) were able to resolve the disk with VLA 8.8 mm observations and came to the conclusion that, due to its small size, large fractional luminosity, and spectral index consistent with blackbody emission, the disk should still retain significant amounts of gas, estimated by the authors to be around $5 M_J$, where M_J is the mass of Jupiter (see Section 2 of Ribas et al. 2018, for further details). If this is the case, the question that naturally arises is: how is it possible that the disk still exists in such a complex environment? Ribas et al. (2018) suggested that the disk is long-lived because it is only evolving due to photoevaporation, with its viscous evolution stopped or significantly slowed down by the torques of both binaries. In this section, we apply our model to this particular case to quantitatively test their hypothesis.

5.1. Modeling the Circumbinary Disk in HD 98800 B

As mentioned above, HD 98800 is a quadruple-star system. However, in order to model the circumbinary disk around Ba–Bb using PLANETALP-B, we consider the outer binary Ab–Aa as a single body. This is a good approximation of its gravitational effect given the large separation between the binaries, and also the orbit of this component has not been resolved yet. Moreover, due to the axial symmetry of our

model, we need to adopt an important simplification: circular and coplanar orbits for both star systems and the disk. We discuss these simplifications in Section 6.

We model the time evolution of the disk around HD 98800 B by considering stars of masses 0.7 and $0.6 M_\odot$ for the system Ba–Bb, so their mass ratio is $q_{\text{Ba-Bb}} = 0.857$, with a total mass of $1.3 M_\odot$ for the system Aa–Ab. We consider two different setups for the orbital parameters. Setup 1 adopts the observed semimajor axes of the system, namely, $a_{\text{Ba-Bb}} = 0.5$ and $a_{\text{A-B}} = 45$ au, but in a circular and coplanar configuration due to the geometrical limitations of our model. For setup 2, we adopt the extreme values $a_{\text{Ba-Bb}} = 0.9$ and $a_{\text{A-B}} = 27$ au, which correspond to the maximum and minimum expansion of the Ba–Bb and B–A orbits (apocenter and pericenter), considering their observed eccentricities of 0.78 and 0.4, respectively, but again, in a circular and coplanar configuration. This range of parameters should capture some of the effects we miss by not having eccentric orbits in the models, allowing us to get realistic estimates of the minimum dissipation timescale of the system.

Unlike in Section 4, we now fix the stellar and orbital parameters of the system and consider different disk parameters, such as different values for M_d and α and different accretion efficiency fractions ϵ , shown in Table 2. As in our previous simulations of Section 4, we keep a fixed exponent for the initial density profile of $\gamma = 1$ and a fixed characteristic radius of $R_0 = 39$ au.

Kastner et al. (2004) were able to measure the X-ray luminosity of HD 98800 B, which is $L_X^{\text{Ba-Bb}} \approx 1.4 \times 10^{29}$ erg s $^{-1}$. This value is an order of magnitude lower than the one we would get with our approach, $L_X^{\text{Ba-Bb}} = L_X^{\text{Ba}} + L_X^{\text{Bb}} \approx 2.53 \times 10^{30}$ erg s $^{-1}$ following Equations (12) and (13), which has important consequences for the disk evolution. As explained in Section 4.1, if only X-ray photoevaporation is considered, and no mass loss due to accretion by tidal streams is allowed, the

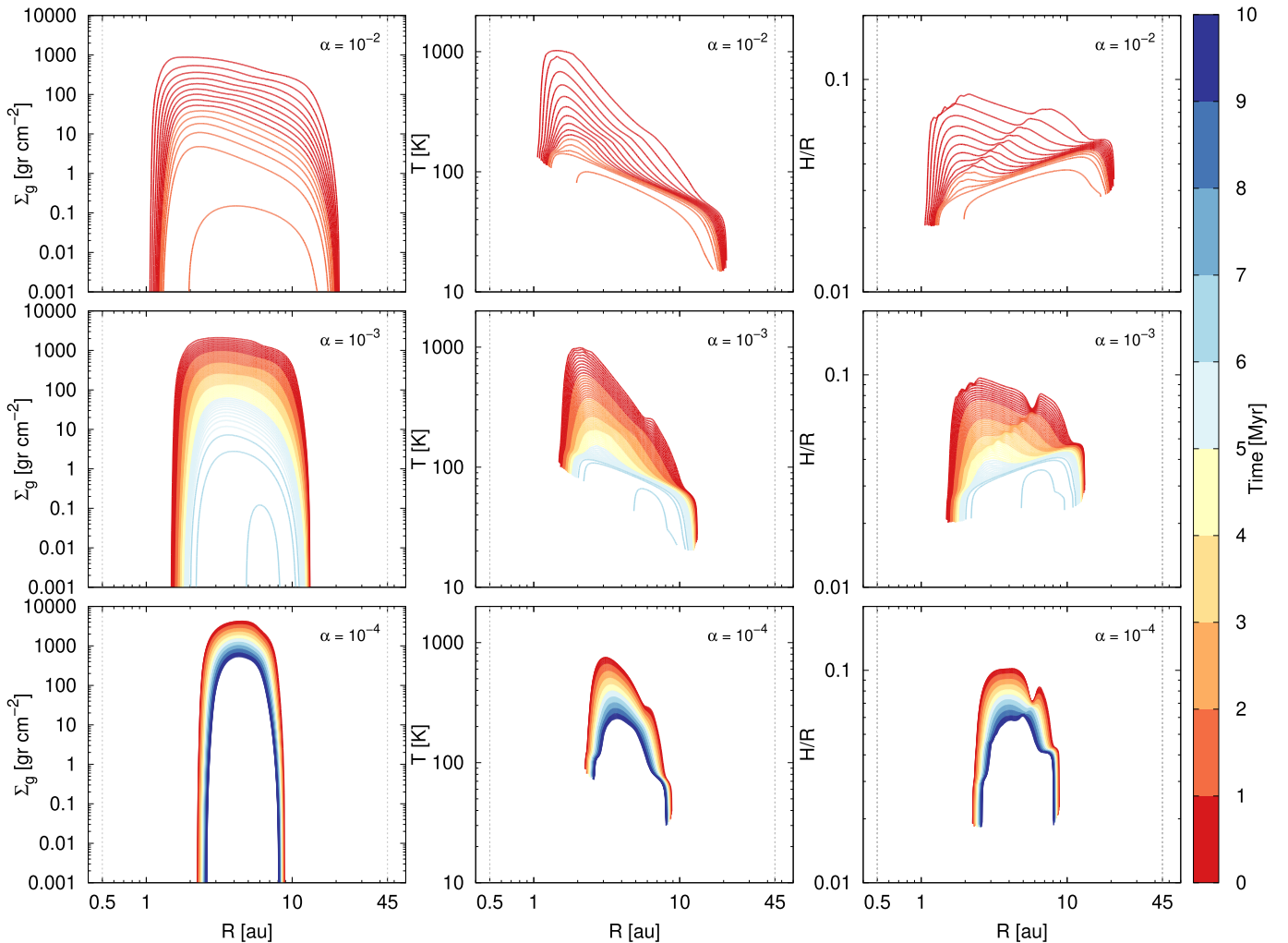


Figure 6. Time evolution of the gas surface density (left column), temperature (middle column), and aspect ratio (right column) for sims 4 (top row), 5 (middle row), and 6 (bottom row), considering accretion via streams with an efficiency of 30% ($\epsilon = 0.3$).

dissipation timescale can be directly estimated without the need of performing simulations. Using $L_X^{\text{Ba-Bb}}$ as measured by Kastner et al. (2004), we obtain disk lifetimes much greater than 10 Myr for disk masses of $M_d = 0.1, 0.05,$ and $0.01 M_\odot$, while, using L_X as computed with Equations (12) and (13), we obtain disk lifetimes of 7.5, 3.7, and 0.7 Myr for the same disk masses. The latter values can be considered as lower limits for the HD 98800 B disk lifetime.

Taking advantage of the fact that this system has a measured X-ray luminosity, we then run the simulations only considering $L_X^{\text{Ba-Bb}}$ as estimated by Kastner et al. (2004). Due to the uncertainties in the mass-loss rates due to stream accretion, we also consider different values for the accretion efficiency ϵ , as shown in Table 2. In Appendix B, we analyze the case in which the accretion efficiency fraction is not set as a constant value but rather as a function of the aspect ratio of the disk, as proposed by Ragusa et al. (2016).

Figure 6 shows the time evolution of the gas surface density (left column), temperature (middle column), and aspect ratio (right column) profiles every 0.1 Myr, represented by the color scale, for sims 4 (top), 5 (middle), and 6 (bottom) of setup 1 (see Table 2) with an accretion efficiency of 30% ($\epsilon = 0.3$). These are the results for a disk of $M_d = 0.05 M_\odot$ with different

α values in the rows. As mentioned before, our simulations end when the disk has completely dissipated, defined as a gas disk mass lower than $10^{-6} M_\odot$, or when it reaches 10 Myr.

The viscosity parameter α , which is the only difference between the simulations of Figure 6, plays an important role in two different aspects. First, it is responsible for shaping the gas surface density, temperature, and disk aspect ratio profiles and, consequently, determining the size and width of the disk. Second, it directly affects the dissipation timescales when some accretion is allowed via streams.

Regarding sizes, the higher the value of α , the wider the disk, which expands in both directions, toward the central binary and outer star. The boundaries for each case, R_c and R_o , can be appreciated in Table 2. These values correspond to the gas disk profile at ~ 0.05 Myr of evolution and measured at $\Sigma_g = 10^{-3} \text{ g cm}^{-2}$ and were computed for the case in which no viscous accretion via streams is allowed. However, they do not change significantly for the cases in which it is allowed; thus, for simplicity, we only show in Table 2 the sizes of the disks for the $\epsilon = 0$ efficiency cases for setups 1 and 2.

The time evolution of the gas surface density profiles for disks with $M_d = 0.01$ and $0.1 M_\odot$ behave in a similar way to the ones described before for $M_d = 0.05 M_\odot$ but with different dissipation timescales.

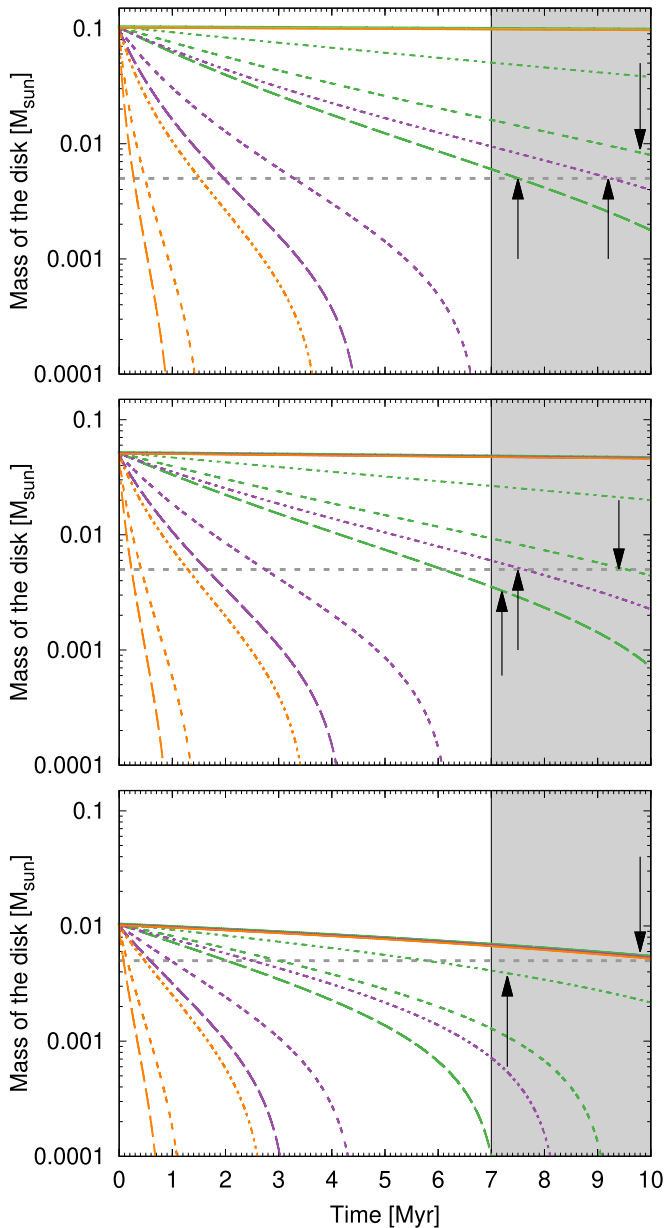


Figure 7. Time evolution of the disk mass in sims 1, 2, and 3 (bottom panel); sims 4, 5, and 6 (middle panel); and sims 7, 8, and 9 (top panel) for $\alpha = 0.0001$ (green), 0.001 (purple), and 0.01 (orange) and accretion efficiencies of 0% (solid lines), 10% (short-dashed lines), 30% (medium-dashed lines), and 50% (long-dashed lines). The black arrows highlight the simulations that fit the estimated mass (horizontal gray dashed line) and age (gray shaded area) of the circumbinary disk HD 98800 B.

Table 2 also shows the dissipation timescales for each of the performed simulations for both setup 1 and setup 2. Those simulations in which the disk dissipates only after the minimum estimated age of HD 98800, 7 Myr, are highlighted in bold for setups 1 and 2. However, only those additionally marked with an asterisk also fit the estimated mass of $\sim 5 M_J$ of the disk around HD 98800 B (Ribas et al. 2018). The latter can also be seen in Figure 7, which shows the time evolution of the mass of the disk for all setup 1 simulations. The bottom panel shows the results for sims 1, 2, and 3 with a disk of $M_d = 0.01 M_\odot$; the middle panel is for sims 4, 5, and 6 with a disk of $M_d = 0.05 M_\odot$; and the top panel is for sims 7, 8, and 9 with a disk of $M_d = 0.1 M_\odot$. Green curves represent simulations with

$\alpha = 0.0001$, purple with $\alpha = 0.001$, and orange with $\alpha = 0.01$. Solid lines represent simulations with accretion efficiencies of 0%, short-dashed lines are 10%, medium-dashed lines are 30%, and long-dashed lines are 50%. The horizontal gray dashed line marks the current estimated mass of HD 98800 B (Ribas et al. 2018), and the shaded area is its probable age. The curves marked with black arrows are the ones highlighted with an asterisk in Table 2.

From Table 2 and Figure 7, it can be deduced that, despite the complex configuration of HD 98800, and assuming our simplified model for HD 98800, we found several cases that would explain the existence of the massive disk after ~ 7 Myr, even with high mass accretion efficiencies via streams and relatively low initial masses. However, moderate-to-low viscosities are needed for the low initial mass cases. It is interesting to remark, though, that the low-viscosity values are the ones that better reproduce some of the ring structures in the DSHARP disks (Dullemond et al. 2018).

As shown by the results in Table 2, for both setup 1 and setup 2, highly viscous disks that are allowed to lose mass via tidal streams with $\geq 10\%$ efficiency dissipate in less than 3.81 Myr, even for the most conservative simulations (the most massive disk in setup 1).

5.2. Could the Potential Disk around HD 98800 A Have Already Been Photoevaporated?

Given the similar total stellar masses for systems A and B, the lack of a disk in system A is intriguing. We do know, however, that the X-ray luminosity of HD 98800 A is about four times higher than that of HD 98800 B (Kastner et al. 2004), which implies a shorter lifetime for a disk around it. Here we will test this idea quantitatively with our model.

We will assume for simplicity that the binary and initial disk in system A have the same parameters as those in system B. It is important to remark that, because system Aa–Ab was classified as an SB1 instead of SB2 (Torres et al. 1995), its actual mass ratio should be lower than that of B. As shown in Section 4.2.1, a smaller value of q_I leads to a faster disk dispersal. Therefore, our choice of $q_A = q_B$, even if not very realistic, is conservative, as it makes the disk in the A system last for longer.

We compute the time evolution of disks around binary A for orbital setup 1, with $L_X^A = 4L_X^B$, and using the parameters of Table 2 that resulted in dissipation timescales longer than 7 Myr for system B (highlighted in bold). Table 3 presents the dissipation timescales for these new simulations. Those in bold represent disks that dissipated in less than 7 Myr, and those additionally marked with an asterisk are the ones that, together with the results of Table 2 (and assuming that both disks, A and B, initially have the same mass), better fit the current mass and age of HD 98800 B and the current nonexistence of a disk around system A. For the disk around system A, moderate- to low-mass disks are needed to allow its dissipation timescale in less than 7 Myr, the minimum age estimated for the quadruple system.

6. Discussion

Here we discuss some important aspects of our model of the evolution of disks in triple hierarchical star systems and the possible influence on planet formation.

Table 3
Dissipation Timescales for the Simulations of Setup 1 for System A

Simulation	Setup 1			
	Efficiency			
	0%	10%	30%	50%
	τ [Myr]	τ [Myr]	τ [Myr]	τ [Myr]
Sim 1	4.20*
Sim 2	4.20*	3.88
Sim 3	4.20*	3.87*	3.26	2.85
Sim 4	>10
Sim 5	>10	6.99*
Sim 6	>10	>10	8.06	6.14*
Sim 7	>10
Sim 8	>10	8.53
Sim 9	>10	>10	>10	7.48

Note. Contrary to Table 2, the resulting timescales shorter than 7 Myr are highlighted in bold, and simulations marked with an asterisk are those that, together with the results of Table 2 (and assuming that both disks, A and B, initially have the same mass), better fit the current mass and age of HD 98800 B and the current nonexistence of a disk around system A.

6.1. General Limitations of Our Model

One of the most important hypotheses in our model, a consequence of its 1D nature, is the axisymmetry of the disk. This characteristic does not properly reproduce the details of the disk structure, which is clearly nonaxisymmetric due to the non-Keplerian potential of the central binary. Even if this approximation might not be the most appropriate to describe the shape of the cavity and the inner regions of circumbinary disks (Dunhill et al. 2015; Miranda et al. 2017; Thun et al. 2017; Thun & Kley 2018; Poblete et al. 2019) heavily affected by the inner binary, it works well in the outer regions, where the binary potential can be approximated by the potential caused by a point mass. In addition, in the particular case of HD 98800 B, we remark that Kennedy et al. (2019) showed that the disk is largely axisymmetrical.

The second important assumption in our model is the circular and coplanar nature of the orbits of the inner binary and the circumbinary disk and external companion with respect to the inner binary. On the one hand, binaries on circular orbits produce the most eccentric cavities (Thun et al. 2017), a feature that we cannot reproduce with our 1D+1D model. Although the development of an eccentric cavity affects gas accretion, which results to be not constant and modulated by the inner binary orbit, we still take this accretion, on average, into account. For our modeling of the disk around HD 98800 B, though, this is not an issue, as the observed binary is not actually circular.

On the other hand, although a full coplanar orbital configuration in a hierarchical triple-star system could seem unlikely at first sight, a very recent analysis of the system TWA3 that hosts a circumbinary disk shows that this could be the case (Czekala et al. 2021). Moreover, we do not expect significant changes in our results for the disk around HD

98800 B, which in fact presents a polar configuration with respect to the inner binary system Ba–Bb (Kennedy et al. 2019), since Franchini et al. (2019) showed that for polar configurations, the main effect on the disk is a reduced inner cavity due to weaker inner torques. It is possible, though, that the irradiation and photoevaporation mechanisms affecting the circumbinary disk are different due to its polar configuration, since the solid angle intercepted by the disk is different. However, models capable of predicting the effects of irradiation and photoevaporation on disks from binary-star systems have not been developed yet, even less if the binary-star systems have a polar orbit with respect to their disks. Thus, we could not predict if this configuration would contribute to a faster disk dispersal or not.

6.2. Effects that Could Accelerate Disk Dispersal

Photoevaporation from the central star is perhaps one of the most important mechanisms affecting mass removal in protoplanetary disks and, as shown previously, is clearly important for circumbinary disks. Disks in hierarchical triple-star systems could have, in addition to the irradiation from the inner binary system, an extra source of X-ray radiation: the external companion. However, as described by Rosotti & Clarke (2018), the irradiation from the external star could be somehow important only if their separation is lower than the radius at which X-ray heating is effective (which is about 100 au; Owen et al. 2012). For the particular case of HD 98800 B, then, the irradiation from the external binary system Aa–Ab could somehow affect its evolution. However, 3D radiation-hydrodynamics simulations that have not yet been developed would be necessary to evaluate this effect.

Another mechanism that could affect disks in general, contributing to a faster disk dispersal, is external photoevaporation from close stellar encounters (Winter et al. 2018) or due to OB massive stars nearby (Clarke 2007; Anderson et al. 2013; Winter et al. 2020). Shadmehri et al. (2018) considered this latter effect in the evolution of circumbinary disks and found that it can significantly affect the disk masses and lifetimes depending on the intensity of the external UV radiation flux. We plan to include this effect in future works. However, it is important to remark that, at least for the Hya association, external photoevaporation does not seem to be relevant, since even with an estimated age of ~ 10 Myr, it still presents disks with detected gas, such as HD 98800 B (Ribas et al. 2018) and TWA 3, where ^{12}CO and ^{13}CO were detected for the first time (Czekala et al. 2021).

6.3. Effects on Planet Formation

One of the most important results of this work is that disks in hierarchical triple-star systems can survive for several megayears, even when allowing gas accretion by tidal streams. This situation, together with the fact that surface density values in triples are, in general, higher than the ones of their circumbinary counterparts (see Figure 2), could favor planet formation even more than in circumbinary disks. In addition, the location of the ice line in triple-star systems is always beyond the corresponding one in the circumbinary disk case, as we show in Section 4.1.1. Thus, for equal initial mass disks and dust-to-gas ratios in circumbinary and triple disks, higher surface densities and larger initial locations of the ice lines could favor the formation of ice cores at larger distances. This

comparison between disks in binaries and triples is analog to the one between circumstellar and circumbinary disks, where the latter have higher gas surface densities. The fact that planet formation in triples, as in binaries, could be favored at larger distances is in line with the idea that planets in circumbinary disks form far away and then migrate inward, parking near the stability limit (Pierens & Nelson 2007; Thun & Kley 2018), as may have happened for the discovered Kepler circumbinary planets.

A possible problem that circumbinary disks in triple-star systems could have in achieving planet formation is their truncation by the external companion. Even in the case of having a disk in a binary and triple with the same initial mass of gas and solids, the truncation of the disk in the triple avoids the continuous supply of dust and pebbles from the outer region of the disk that could be quickly lost due to radial drift, unlike what happens in circumbinary disks not affected by an external companion. This situation was recently studied by Zagaria et al. (2021), who found that the dust in circumstellar disks around one of the stars in a binary-star system drifts faster than in disks not affected by an outer stellar companion.

Nevertheless, an interesting situation could occur for disks with large a_I (see panels T6 and T7 of Figure 5) and low viscosities (see bottom row of Figure 6). In these cases, the gas surface density shows quasi-Gaussian radial profiles with a well-defined maximum. As was recently shown by Guilera et al. (2020), a maximum in the gas surface density is related to a pressure maximum, and it represents a preferential location for the dust/pebble trap, planetesimal formation by streaming instability, and planet formation by hybrid accretion of pebbles and planetesimals. Moreover, the well-defined pressure maximum can act as a planet migration trap, thus favoring planet formation.

7. Conclusions

We present PLANETALP-B, a 1D+1D model able to compute the time evolution of the gaseous component of circumbinary disks in triple hierarchical stellar systems in circular and coplanar orbits. Our model considers viscous accretion, irradiation from the central binary, and X-ray photoevaporation. This model can also be applied to the study of the evolution of circumbinary disks around close-in binaries or circumstellar disks around one of the stars in a wide binary-star system. The general goal of this work is to compare the evolution of circumbinary disks in binaries and triple hierarchical stellar systems and characterize their particular features and lifetimes. A particular goal is to try to understand how it is possible that some disks in these complex stellar environments survive for longer than typical protoplanetary disks.

Our main results are briefly summarized as follows.

1. The gas disk profiles in binaries and triples are quite different, and these differences are mainly related to the size of the inner cavities and outer radius of the disks. While disks in triples evolve almost confined in a radial range, disks in binaries migrate and expand radially.
2. Disks in triple-star systems dissipate faster than their circumbinary counterparts when accretion by tidal streams is considered as a natural consequence of their higher surface density profiles. However, the difference in their dissipation timescales is only about 20%.
3. Disks in triple-star systems last for longer timescales than their circumstellar counterparts, even when considering an efficiency for the accretion by tidal streams of 30%.
4. Disks in triple-star systems dissipate faster for lower values of q_I , though the differences are not significant. The opposite happens for lower values of q_{II} .
5. Higher values of a_I provoke larger inner cavities. However, the mass-loss rate due to viscous accretion by tidal streams remains similar as a consequence of a balance produced between the gas surface density and the viscosity. This effect compensates for the dissipation timescales, which are almost the same for the considered cases.
6. The main effect of higher values of a_{II} is that the dissipation timescales are longer. Disks with $a_{II} > 500$ au tend to dissipate in the same timescales as their corresponding circumbinary disks.
7. We are able to explain the estimated age and mass of HD 98800 B for certain disk parameters (inter-mediate to high mass disks and moderate to low viscosities) and as a consequence of the disk evolving mainly by fotoevaporation, as suggested by Ribas et al. (2018). Simultaneously, we are also able to explain the absence of a disk around binary system A.

Thus, our study helps characterize the main features of disks in hierarchical triple-star systems and sheds light on the process of planet formation in these complex environments.

We thank the anonymous referee for the enthusiasm about our work and the editor, Gregory Herczeg, for his useful comments. M.P.R. acknowledges financial support provided by FONDECYT grant 3190336. M.P.R. thanks Richard Alexander for useful discussions on some aspects of the model. M.P.R., O.M.G., J.C., and A.B. acknowledge support by ANID—Millennium Science Initiative Program—NCN19_171. O.M.G. is partially support by PICT 2018-0934 from ANPCyT, Argentina. O.M.G. and M.M.M.B. are partially supported by PICT 2016-0053 from ANPCyT, Argentina. This project has received funding from the European Union’s Horizon 2020 research and innovation program under Marie Skłodowska-Curie grant agreement No. 210021. A.B. acknowledges support from FONDECYT Regular 1190748.

Appendix A

Validation of Our 1D+1D Model: Vertical Structure and Gas Evolution for Circumbinary Disks

In order to validate our 1D+1D model for the vertical structure and time evolution of the gas in circumbinary disks added in PLANETALP-B, we compare our results against those of Vartanyan et al. (2016), only for their case with $M_d = 0.1 M_\odot$ (their Figure 5 and 6).

We first compute the vertical structure of the disk using the same stellar and disk parameters they considered but computing the irradiation of the disk following our Equations (9) and (10). The disk and stellar parameters are $a_I = 0.2$ au, $\alpha = 0.01$, $M_d = 0.1 M_\odot$, $L_I = 2 L_\odot$, $q_I = 1$, and central binary of total mass $M_I = 1 M_\odot$.

As was also noticed by Shadmehri et al. (2018), the binary torque equation in Vartanyan et al. (2016) is a bit different from the classical one from Armitage & Natarajan (2002). In order to properly compare our model with that of Vartanyan et al. (2016),

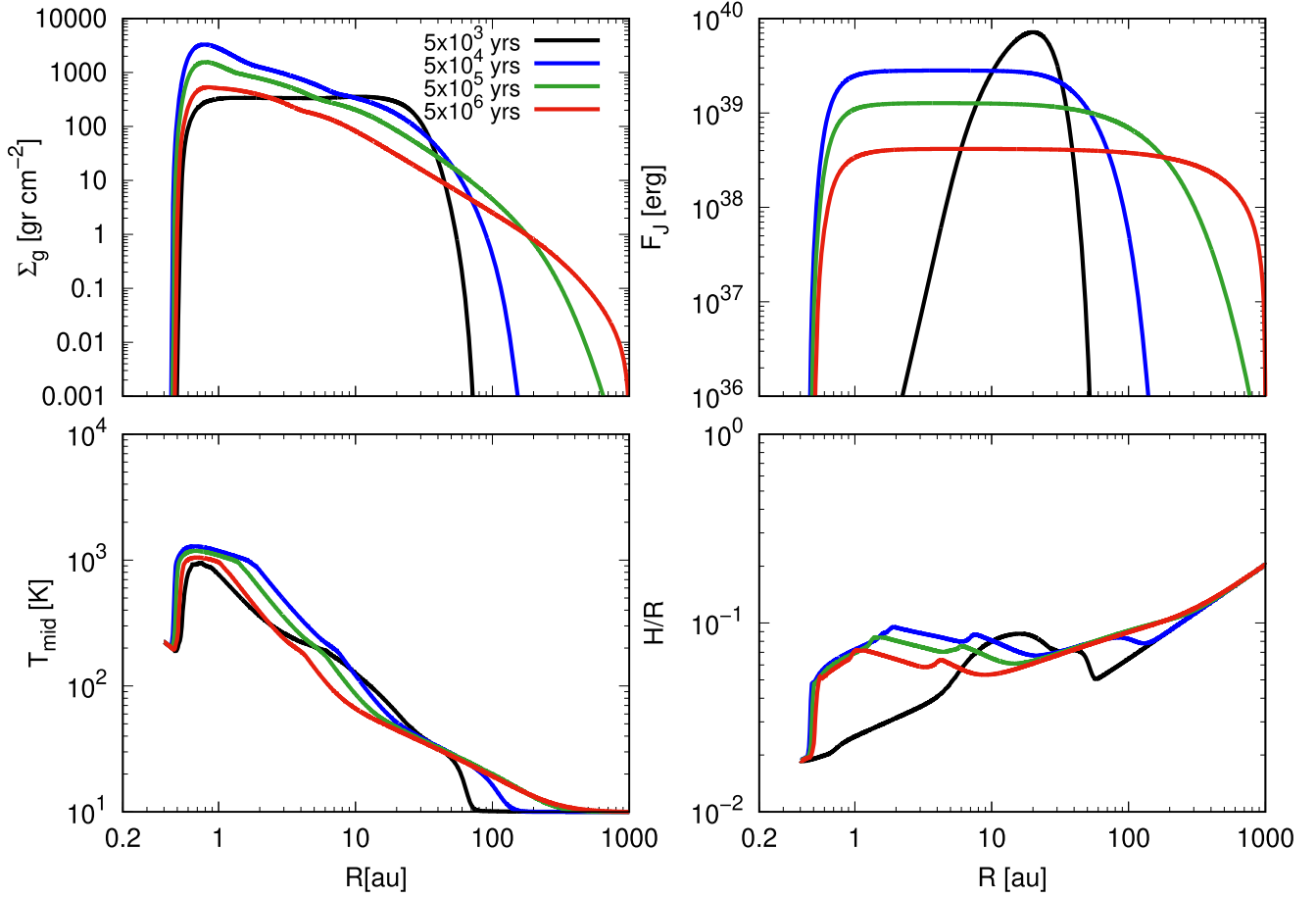


Figure 8. Time evolution of the gas surface density (top left), flux (top right), midplane temperature (bottom left), and aspect ratio (bottom right) for the comparison case with Vartanyan et al. (2016; see their Figures 5 and 6): $M_1 = 1 M_\odot$, $q = 1$, $a_1 = 0.2$ au, $r_{\text{in}} = 0.2$ au, $\alpha = 0.01$, and $M_d = 0.1 M_\odot$.

we use the same expression they used, with a factor $f = 2 \times 10^{-3}$ (see their Equation (3)).

We then compute the time evolution of the gaseous component by solving Equation (11) without photoevaporation from the central star, that is, $\dot{\Sigma}_w(R) = 0$. The initial profile used by Vartanyan et al. (2016) is a narrow initial peak distribution in the shape of a ring given by

$$\Sigma_g = \frac{M_d}{(2\pi)^{3/2} R_0 \sigma_r} \exp\left(-\frac{(R - R_0)^2}{2\sigma_r^2}\right), \quad (\text{A1})$$

where $R_0 = 20$ au is the initial radius of the disk, and $\sigma_r = 2$ au is its width.

Figure 8 shows the gas surface density (top left panel); viscous angular momentum flux profiles, computed as $F_J = 3\pi\nu\Sigma l$, with $l = \Omega R^2$ the specific angular momentum (top right panel); midplane temperature (bottom left panel); and aspect ratio (bottom right panel) for the comparison case and at the same times showed by Vartanyan et al. (2016). The flux profiles can be compared with their Figure 3, and the gas and temperature profiles can be compared with Figure 6 of their work. The aspect ratio in Vartanyan et al. (2016) is only shown for a disk of $M_d = 0.05 M_\odot$ (see their Figure 11); however, it presents very similar characteristics to our case of $M_d = 0.1 M_\odot$.

As in Vartanyan et al. (2016), our disks would also be prone to self-shadowing caused by the tidal and viscous heating enhancement of the midplane temperature and thus the aspect

ratio of the inner regions of the disk. This effect can be clearly appreciated in the bottom left and right panels of Figure 8, where beyond ~ 20 au, H/R presents a flared structure, but between ~ 1 and ~ 20 au, H/R increases as R gets smaller. This effect could change the temperature in this region, which could be lower, in fact. As pointed out by Vartanyan et al. (2016), taking into account the self-shadowing in 1D+1D models is extremely hard and completely outside the scope of this work.

In general, our results look very similar to those of Vartanyan et al. (2016), despite some minor differences mainly related to the fact that our irradiation model is different. We particularly reproduce quite well the inner cavity of the disk, which expands almost up to ~ 0.5 au, between two and three times the binary separation, and the very early plateau distribution in the flux.

Appendix B

Accretion Efficiency as a Function of the Aspect Ratio

The evolution of circumbinary disks, studied by means of 1D models, predicts that viscous accretion of material is not possible. As mentioned before, this result is due to the particular way of modeling the viscous torques. Instead, 2D and 3D simulations have shown that viscous accretion can happen via gas tidal streams inside the cavity with accretion rates that could be similar to or higher than those of single-star systems. However, this scenario can drastically change when the disks become thin. Ragusa et al. (2016) found that when the

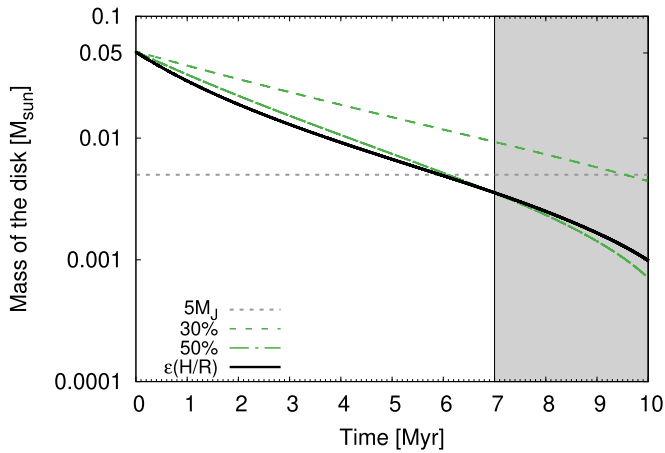


Figure 9. Time evolution of the disk of sim 6–setup 1 (see Table 2). The green short- and long-dashed curves are computed with a fixed value for the accretion efficiency of 30% and 50%, respectively. The solid black curve is computed with an accretion efficiency fraction that depends on the aspect ratio of the disk by following Equation (B1).

aspect ratio of the disk (H/R) is $\gtrsim 0.1$, the accretion efficiency is not affected by the tidal torques of the inner binary; however, for thinner disks with $H/R < 0.1$, the accretion efficiency linearly decays as

$$\epsilon(H/R) \approx \begin{cases} 10(H/R) & \text{if } H/R \leq 0.1 \\ 1 & \text{if } H/R > 0.1. \end{cases} \quad (\text{B1})$$

Here we again compute the time evolution of the circumbinary disk of sim 6–setup 1 (see Table 2), but instead of considering a fixed value for the accretion efficiency, as we did in Section 5.1, we follow Equation (B1).

Figure 9 shows the time evolution of the mass of the disk of sim 6 (solid black line) computed following Equation (B1) and compared to the cases computed with a fixed value of the accretion efficiency of 30% ($\epsilon = 0.3$) and 50% ($\epsilon = 0.5$), shown by short- and long-dashed lines, respectively. As can be seen, the more realistic approach derived by Ragusa et al. (2016) is in good agreement with an accretion efficiency of $\sim 50\%$ regardless of the aspect ratio of the disk.

ORCID iDs

María Paula Ronco <https://orcid.org/0000-0003-1385-0373>
 Octavio M. Guilera <https://orcid.org/0000-0001-8577-9532>
 Jorge Cuadra <https://orcid.org/0000-0003-1965-3346>
 Marcelo M. Miller Bertolami <https://orcid.org/0000-0001-8031-1957>
 Nicolás Cuello <https://orcid.org/0000-0003-3713-8073>
 Pedro Poblete <https://orcid.org/0000-0003-0974-8747>
 Amelia Bayo <https://orcid.org/0000-0001-7868-7031>

References

Akeson, R. L., Jensen, E. L. N., Carpenter, J., et al. 2019, *ApJ*, 872, 158
 Alexander, R. 2012, *ApJL*, 757, L29
 Alexander, R. D., Clarke, C. J., & Pringle, J. E. 2006, *MNRAS*, 369, 229
 Alibert, Y., Mordasini, C., Benz, W., & Winisdoerffer, C. 2005, *A&A*, 434, 343
 ALMA Partnership, Brogan, C. L., Pérez, L. M., et al. 2015, *ApJL*, 808, L3
 Alves, F. O., Caselli, P., Girart, J. M., et al. 2019, *Sci*, 366, 90
 Anderson, K. R., Adams, F. C., & Calvet, N. 2013, *ApJ*, 774, 9
 Andrews, S. M., Wilner, D. J., Hughes, A. M., Qi, C., & Dullemond, C. P. 2010, *ApJ*, 723, 1241

Armitage, P. J., & Natarajan, P. 2002, *ApJL*, 567, L9
 Artymowicz, P., & Lubow, S. H. 1994, *ApJ*, 421, 651
 Artymowicz, P., & Lubow, S. H. 1996, *ApJL*, 467, L77
 Baraffe, I., Homeier, D., Allard, F., & Chabrier, G. 2015, *A&A*, 577, A42
 Barrado Y Navascués, D. 2006, *A&A*, 459, 511
 Bate, M. R. 2018, *MNRAS*, 475, 5618
 Boden, A. F., Sargent, A. I., Akeson, R. L., et al. 2005, *ApJ*, 635, 442
 Bonavita, M., & Desidera, S. 2020, *Galax*, 8, 16
 Cieza, L. A., Padgett, D. L., Allen, L. E., et al. 2009, *ApJL*, 696, L84
 Cieza, L. A., Ruíz-Rodríguez, D., Hales, A., et al. 2019, *MNRAS*, 482, 698
 Clarke, C. J. 2007, *MNRAS*, 376, 1350
 Correia, S., Zinnecker, H., Ratzka, T., & Sterzik, M. F. 2006, *A&A*, 459, 909
 Cox, E. G., Harris, R. J., Looney, L. W., et al. 2017, *ApJ*, 851, 83
 Cuadra, J., Armitage, P. J., Alexander, R. D., & Begelman, M. C. 2009, *MNRAS*, 393, 1423
 Czekala, I., Ribas, Á., Cuello, N., et al. 2021, *ApJ*, 912, 6
 del Valle, L., & Escala, A. 2012, *ApJ*, 761, 31
 D’Orazio, D. J., Haiman, Z., & MacFadyen, A. 2013, *MNRAS*, 436, 2997
 Duchêne, G., & Kraus, A. 2013, *ARA&A*, 51, 269
 Ducourant, C., Teixeira, R., Galli, P. A. B., et al. 2014, *A&A*, 563, A121
 Dullemond, C. P., Birnstiel, T., Huang, J., et al. 2018, *ApJL*, 869, L46
 Dunhill, A. C., Cuadra, J., & Dougados, C. 2015, *MNRAS*, 448, 3545
 Ercolano, B., & Owen, J. E. 2010, *MNRAS*, 406, 1553
 Farris, B. D., Duffell, P., MacFadyen, A. I., & Haiman, Z. 2014, *ApJ*, 783, 134
 Fedele, D., van den Ancker, M. E., Henning, T., Jayawardhana, R., & Oliveira, J. M. 2010, *A&A*, 510, A72
 Fontecilla, C., Haiman, Z., & Cuadra, J. 2019, *MNRAS*, 482, 3383
 Franchini, A., Lubow, S. H., & Martin, R. G. 2019, *ApJL*, 880, L18
 Gorti, U., Dullemond, C. P., & Hollenbach, D. 2009, *ApJ*, 705, 1237
 Guilera, O. M., Cuello, N., Montesinos, M., et al. 2019, *MNRAS*, 486, 5690
 Guilera, O. M., Miller Bertolami, M. M., & Ronco, M. P. 2017, *MNRAS*, 471, L16
 Guilera, O. M., Sándor, Z., Ronco, M. P., Venturini, J., & Miller Bertolami, M. M. 2020, *A&A*, 642, A140
 Hirsh, K., Price, D. J., Gonzalez, J.-F., Ubeira-Gabellini, M. G., & Ragusa, E. 2020, *MNRAS*, 498, 2936
 Jiménez, M. A., & Masset, F. S. 2017, *MNRAS*, 471, 4917
 Kastner, J. H., Huenemoerder, D. P., Schulz, N. S., et al. 2004, *ApJL*, 605, L49
 Kastner, J. H., Zuckerman, B., Weintraub, D. A., & Forveille, T. 1997, *Sci*, 277, 67
 Kennedy, G. M., Matrà, L., Facchini, S., et al. 2019, *NatAs*, 3, 230
 Kraus, A. L., Ireland, M. J., Hillenbrand, L. A., & Martinache, F. 2012, *ApJ*, 745, 19
 Kraus, S., Kreplin, A., Young, A. K., et al. 2020, *Sci*, 369, 1233
 Kunitomo, M., Ida, S., Takeuchi, T., et al. 2021, *ApJ*, 909, 109
 Lambrechts, M., Johansen, A., & Morbidelli, A. 2014, *A&A*, 572, A35
 Lodato, G., Nayakshin, S., King, A. R., & Pringle, J. E. 2009, *MNRAS*, 398, 1392
 MacFadyen, A. I., & Milosavljević, M. 2008, *ApJ*, 672, 83
 Ribas, Á., Macías, E., Espaillat, C. C., & Duchêne, G. 2018, *ApJ*, 865, 77
 Manara, C. F., Tazzari, M., Long, F., et al. 2019, *A&A*, 628, A95
 Martin, D. V. 2018, in *Handbook of Exoplanets*, ed. H. J. Deeg & J. A. Belmonte (Berlin: Springer), 156
 Marzari, F., & Thebault, P. 2019, *Galax*, 7, 84
 Migaszewski, C. 2015, *MNRAS*, 453, 1632
 Miranda, R., Muñoz, D. J., & Lai, D. 2017, *MNRAS*, 466, 1170
 Olofsson, J., Juhász, A., Henning, T., et al. 2012, *A&A*, 542, A90
 Owen, J. E., Clarke, C. J., & Ercolano, B. 2012, *MNRAS*, 422, 1880
 Owen, J. E., Ercolano, B., & Clarke, C. J. 2011, *MNRAS*, 412, 13
 Paardekooper, S.-J., Baruteau, C., & Kley, W. 2011, *MNRAS*, 410, 293
 Papaloizou, J., & Pringle, J. E. 1977, *MNRAS*, 181, 441
 Petrovich, C., & Rafikov, R. R. 2012, *ApJ*, 758, 33
 Pflanzner, S., Steinhausen, M., & Menten, K. 2014, *ApJL*, 793, L34
 Pichardo, B., Sparke, L. S., & Aguilar, L. A. 2005, *MNRAS*, 359, 521
 Picogna, G., Ercolano, B., Owen, J. E., & Weber, M. L. 2019, *MNRAS*, 487, 691
 Pierens, A., & Nelson, R. P. 2007, *A&A*, 472, 993
 Poblete, P. P., Cuello, N., & Cuadra, J. 2019, *MNRAS*, 489, 2204
 Prato, L., Ghez, A. M., Piña, R. K., et al. 2001, *ApJ*, 549, 590
 Preibisch, T., Kim, Y.-C., Favata, F., et al. 2005, *ApJS*, 160, 401
 Pringle, J. E. 1981, *ARA&A*, 19, 137
 Rafikov, R. R. 2016, *ApJ*, 827, 111
 Rafikov, R. R., & Petrovich, C. 2012, *ApJ*, 747, 24
 Ragusa, E., Alexander, R., Calcino, J., Hirsh, K., & Price, D. J. 2020, *MNRAS*, 499, 3362
 Ragusa, E., Lodato, G., & Price, D. J. 2016, *MNRAS*, 460, 1243

- Reipurth, B., Clarke, C. J., Boss, A. P., et al. 2014, in *Protostars and Planets VI*, ed. H. Beuther et al. (Tucson, AZ: Univ. Arizona Press), 267
- Ronco, M. P., Guilera, O. M., & de Elía, G. C. 2017, *MNRAS*, 471, 2753
- Rosotti, G. P., & Clarke, C. J. 2018, *MNRAS*, 473, 5630
- Schwarz, R., Funk, B., Zechner, R., & Bazsó, Á. 2016, *MNRAS*, 460, 3598
- Shadmehri, M., Ghoreyshi, S. M., & Alipour, N. 2018, *ApJ*, 867, 41
- Shakura, N. I., & Sunyaev, R. A. 1973, *A&A*, 24, 337
- Soderblom, D. R., Henry, T. J., Shetrone, M. D., Jones, B. F., & Saar, S. H. 1996, *ApJ*, 460, 984
- Tang, Y., MacFadyen, A., & Haiman, Z. 2017, *MNRAS*, 469, 4258
- Tazzari, M., & Lodato, G. 2015, *MNRAS*, 449, 1118
- Thun, D., & Kley, W. 2018, *A&A*, 616, A47
- Thun, D., Kley, W., & Picogna, G. 2017, *A&A*, 604, A102
- Tobin, J. J., Kratter, K. M., Persson, M. V., et al. 2016, *Natur*, 538, 483
- Tokovinin, A., Mason, B. D., & Hartkopf, W. I. 2014, *AJ*, 147, 123
- Tokovinin, A. A. 1999, *AstL*, 25, 669
- Torres, C. A. O., Quast, G. R., Melo, C. H. F., & Sterzik, M. F. 2008, in *Handbook of Star Forming Regions: The Southern Sky*, ed. B. Reipurth, Vol. 5 (San Francisco, CA: ASP), 757
- Torres, G., Stefanik, R. P., Latham, D. W., & Mazeh, T. 1995, *ApJ*, 452, 870
- Vartanyan, D., Garmilla, J. A., & Rafikov, R. R. 2016, *ApJ*, 816, 94
- Venturini, J., Guilera, O. M., Ronco, M. P., & Mordasini, C. 2020a, *A&A*, 644, A174
- Venturini, J., Ronco, M. P., & Guilera, O. M. 2020b, *SSRv*, 216, 86
- Winter, A. J., Clarke, C. J., Rosotti, G., et al. 2018, *MNRAS*, 478, 2700
- Winter, A. J., Kruijssen, J. M. D., Longmore, S. N., & Chevance, M. 2020, *Natur*, 586, 528
- Zagaria, F., Rosotti, G. P., & Lodato, G. 2021, *MNRAS*, 504, 2235
- Zurlo, A., Cieza, L. A., Pérez, S., et al. 2020, *MNRAS*, 496, 5089